

## Investigation of Fluid-dynamics and Mass-transfer in a bubbly mixing layer by Euler-Euler simulation

Kappelt, C.; Rzehak, R.;

Originally published:

September 2022

**Chemical Engineering Science 264(2022), 118147**

DOI: <https://doi.org/10.1016/j.ces.2022.118147>

Perma-Link to Publication Repository of HZDR:

<https://www.hzdr.de/publications/Publ-35557>

Release of the secondary publication  
on the basis of the German Copyright Law § 38 Section 4.

CC BY-NC-ND

1 Investigation of Fluid-dynamics and Mass-transfer in a Bubbly Mixing Layer by  
2 Euler-Euler Simulation

3 Carolin Kappelt, Roland Rzehak\*

4  
5  
6 Helmholtz-Zentrum Dresden – Rossendorf, Institute of Fluid Dynamics,  
7 Bautzner Landstrasse 400, D-01328 Dresden, Germany

8  
9  
10 **Abstract**

11 Mass transfer in bubbly flows is a field of obvious technological importance. On industrially  
12 relevant scales it may be studied by simulations based on the Euler-Euler two-fluid model,  
13 which however requires closure models for the interfacial exchange processes. Despite  
14 recently increased efforts, modelling of the exchange of mass between the phases is still much  
15 less developed than the corresponding exchange of momentum. The present study compares  
16 several proposed models for the mass transfer coefficient using a previously established set  
17 of closure relations for the purely fluid dynamical part of the problem. A set of experimental  
18 data for the absorption of O<sub>2</sub> into water in a bubbly mixing layer from the literature is used to  
19 assess their relative merits. A model for the pertinent material properties of this system has  
20 been assembled from available measurements. A rather sensitive dependence of the amount  
21 of absorbed O<sub>2</sub> is found on the pressure, which varies with the hydrostatic head above the  
22 test section.

23  
24 **Keywords:** mass-transfer, dispersed gas-liquid multiphase flow, Euler-Euler two-fluid model,  
25 closure relations, CFD simulation, model validation

26  
27  

---

\* Corresponding author. E-mail: r.rzehak@hzdr.de

## 28 1 INTRODUCTION

29 Mass-transfer between gas bubbles and the liquid surrounding them is an important  
30 phenomenon in chemical engineering and biotechnology as well as cleaning and purification  
31 processes in diverse fields of application. In comparison to merely fluid dynamical problems,  
32 the modeling of mass transfer phenomena in bubbly flows is developed much less. On the  
33 scale of technical equipment, simulations are feasible by means of the Eulerian framework of  
34 multiphase flow. For practical application this requires a closure relation for the mass transfer  
35 coefficient, the suitability of which has to be validated by comparing the simulations results  
36 to experimental data.

37 A review of earlier work in this field has been given in Rzehak and Krepper (2016) for purely  
38 physical mass transfer and in Krauß and Rzehak (2018, 2017) for the case with an  
39 accompanying chemical reaction. The topic has received continued high interest since then,  
40 especially with a focus on reactive systems such as CO<sub>2</sub> in aqueous NaOH (Hori et al. 2020) or  
41 NO in aqueous Fe<sup>II</sup> complexes (Hlawitschka et al. 2017a), comprising both experiments  
42 (Kipping et al. 2020, Kovats et al. 2018) and simulations by the Euler-Euler and Euler-Lagrange  
43 methods (Taborda and Sommerfeld 2021, Hlawitschka et al. 2017b). Despite these recent  
44 advances, the quest for a well-validated and broadly applicable model for the bubbles' mass  
45 transfer coefficient remains an ongoing venture (Solsvik 2018).

46 For data serving the purpose of model validation it is essential that the concentration, phase  
47 fraction, and velocity fields are available with a decent resolution over the flow domain. In  
48 addition, measurements of the bubble size are required as well, since this quantity appears  
49 in virtually all of the closure models used in Euler-Euler simulations. Furthermore, it would be  
50 highly desirable that the data also contain some variation of this parameter so that a  
51 meaningful comparison between different models can be made. Sources of such data for  
52 cases involving mass transfer are much scarcer than for purely fluid dynamical problems. For  
53 the present investigation, the work of Ayed et al. (2007) is considered.

54 The fluid dynamic modeling used in the present work employs a baseline model established  
55 in Rzehak and Krepper (2013) and thoroughly validated in a number of studies since then for  
56 simple bubbly pipe flows and bubble columns (e.g. Rzehak et al. 2017, 2017a, 2015, Fleck and  
57 Rzehak 2019, Rzehak and Kriebitzsch 2015, Rzehak and Krepper 2015, 2013a, Ziegenhein et  
58 al. 2017, 2015, 2013), but also for more complex applications such as an airlift-column (Liao  
59 et al. 2016), a helical static mixer (Zidouni et al. 2015) and a stirred tank (Shi and Rzehak  
60 2018). Since this model was shown to give consistently good agreement with experimental  
61 data over a significant range of conditions, it provides a reliable basis to describe the fluid  
62 dynamics of bubbly flows. For the present investigation, two correlations for the drag force  
63 are compared corresponding to different water quality. The general description of mass  
64 transfer follows Rzehak and Krepper (2016). For the mass transfer coefficient several  
65 correlations applied in previous works are evaluated. In the experiments of (Ayed et al. 2007)  
66 the transferred species was oxygen, O<sub>2</sub>, and a model for the pertinent material properties is  
67 assembled from literature sources.

68 Detailed local information is available in the work of Ayed et al. (2007) in the form of lateral  
69 profiles taken at several axial locations, but only a single test condition has been considered.  
70 In addition to the concentration of dissolved O<sub>2</sub> in the liquid phase, also fluid dynamical  
71 observables have been measured. This provides in addition to the investigation of mass  
72 transfer models also a further qualification of the fluid dynamical part of the model for a  
73 configuration that is more complex than simple pipe flows or bubble columns.

74 In addition to the experiments, also Euler-Euler simulations have been presented by Ayed et  
75 al. (2007). As will be discussed, the closure models used for the fluid dynamical part are  
76 comparable to the present ones. However, upon careful inspection the source of the assumed  
77 correlation for the mass transfer coefficient and its applicability to the present case is unclear.  
78 Moreover, it is found that pressure has a significant effect on the amount of absorbed O<sub>2</sub>. This  
79 makes the actual water level in the reservoir at the top of the column an important variable,  
80 which highlights the importance of complete specifications for test cases to be used in model  
81 validation.

82 The paper is organized as follows: A summary of the experiments is given in section 2. The  
83 applied models are described in section 3. Emphasis is put on the mass transfer part in section  
84 3.1. For the fluid dynamical part a brief summary and a guide to previous work is given in  
85 section 3.2. The material model is furnished in section 3.3. In section 4, the simulation results  
86 are presented and comparison is made to the measurements. Finally, discussion is offered in  
87 section 5.

88

89 2 SUMMARY OF EXPERIMENTAL DATA

90 Ayed et al. (2007) considered bubbly flow in a mixing layer as sketched in

91 Figure 1. The test section was a vertically oriented rectangular flow channel. The inlet at the  
92 bottom was composed of two square regions separated by a splitter plate. Inlet 1 was  
93 supplied with pure liquid while at inlet 2 a sparger consisting of 576 needles distributed evenly  
94 over the inlet area injected gas into the flowing liquid. The set values of liquid volume flux and  
95 gas fraction are summarized in Table 1. Materials used were pure oxygen ( $O_2$ ) for the gas and  
96 water for the liquid. A small amount of oxygen corresponding to a mass fraction of  $Y_L^{O_2} =$   
97  $9.96e-6$  was initially dissolved in the water. No statement concerning the water quality (clean  
98 or contaminated) is available. Temperature and pressure were at ambient values. However  
99 closer inspection of the setup revealed that there is a 0.6 m deep reservoir on top of the test  
100 section which is filled to an unknown level (Roig and Larue de Tournemine 2007, Figure 2).  
101 This leaves some uncertainty at which height precisely the system is actually open to the  
102 atmosphere.

103

104 Figure 1: Sketch of the geometry for the  
105 test from Ayed et al. (2007).

106

107

108

109

110

111

112

113

114

115

116

117

118

119

120

121

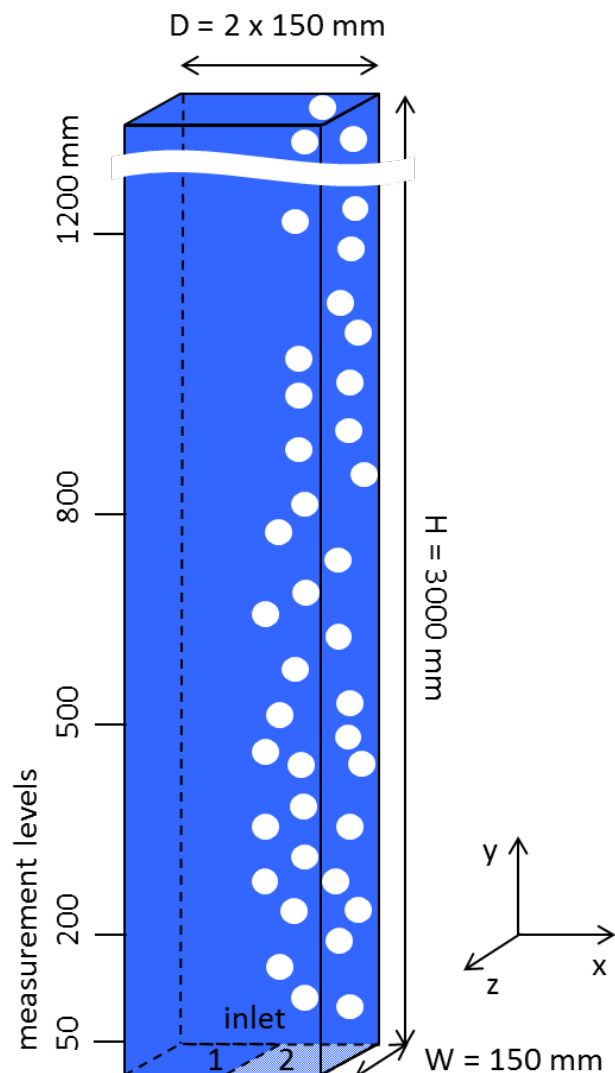
122

123

124

125

126



test case	$J_L(in1)$	$J_L(in2)$	$\alpha_G(in1)$	$\alpha_G(in2)$	$Y_L^{O_2}(in1)$	$Y_L^{O_2}(in2)$	$\langle d_B \rangle$
Ayed et al. (2007)	m/s	m/s	%	%	-	-	mm
-	0.57	0.29	0.0	2.0	9.96e-6	9.96e-6	1.8

127

128 Table 1: Summary of parameters for the test of Ayed et al. (2007).

129

130 Measurements were taken along lateral profiles in the mid-plane of the channel at five axial  
131 locations above the inlet as indicated in

132 Figure 1. Measured quantities were gas fraction, bubble size, mean axial liquid velocity, axial  
133 liquid velocity fluctuations, relative velocity between gas and liquid, and oxygen  
134 concentration in the liquid. Oxygen concentration was measured by a Clark electrode probe.  
135 For the observables pertaining to the gas phase a two-point optical-fiber probe was used,  
136 while the liquid phase velocity was determined by a hot-film probe. Concerning the bubble  
137 size only minor variation with height was found, which indicates that processes of bubble-  
138 coalescence and -breakup are at most of minor importance. Averaging over all levels gave an  
139 average value of  $d_B = 1.8$  mm with a standard deviation of 0.3 mm.

140

141 3 DESCRIPTION OF PHYSICAL MODELS

142 The main focus here is on the mass transfer part of the model, which is covered in section 3.1.  
 143 A concise summary of the fluid dynamical part of the model is given in section 3.2, because  
 144 this part was chosen to exactly match a baseline model that was validated in a number of  
 145 previous studies. Full details of this model have been given e.g. in Rzehak and Krepper (2013)  
 146 or Rzehak et al. (2017). A material model for the system of O<sub>2</sub> and water is finally presented  
 147 in section 3.3.

148 3.1 Mass Transfer

149 To describe mass transfer phenomena, equations for the concentration of the transferred  
 150 species, which appears as a solute in both phases, are required. These are summarized as

$$\frac{\partial}{\partial t}(\alpha_G \rho_G Y_G^A) + \nabla \cdot (\alpha_G \rho_G \mathbf{u}_G Y_G^A) = \nabla \cdot (\alpha_G \rho_G D_G^{eff,A} \nabla Y_G^A) + \Gamma_G^A \quad (1)$$

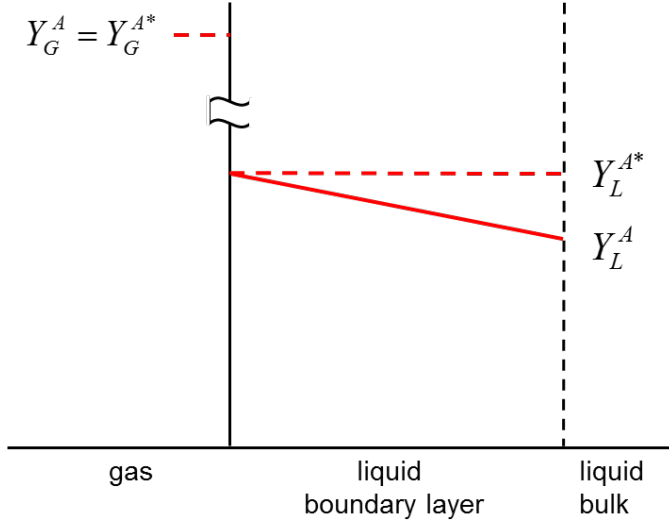
$$\frac{\partial}{\partial t}(\alpha_L \rho_L Y_L^A) + \nabla \cdot (\alpha_L \rho_L \mathbf{u}_L Y_L^A) = \nabla \cdot (\alpha_L \rho_L D_L^{eff,A} \nabla Y_L^A) + \Gamma_L^A . \quad (2)$$

151 Here, A denotes the transferred species,  $Y^A = \rho^A / \rho$  is its mass fraction and  $\rho = \sum_X \rho^X$  is the  
 152 density of the multi-component mixture of which each phase consists. No separate equations  
 153 are needed for the solute, since its mass fraction can be calculated from the constraint  
 154  $\sum_X Y^X = 1$ . Care should be taken not to confuse the mass concentration of a species in a  
 155 mixture with the thermodynamic density of the pure substance although unfortunately the  
 156 same letter  $\rho$  is conventionally used to denote both. The phase fraction  $\alpha$  and phasic velocity  
 157  $\mathbf{u}$  are obtained from the fluid dynamical part of the model (see section 3.2). The mass transfer  
 158 sources for both phases are related as  $\Gamma_G^A = -\Gamma_L^A$  to satisfy mass conservation and their sign  
 159 is such that for absorption  $\Gamma_L^A > 0$ . Further models are needed for the effective diffusion  
 160 coefficient  $D^{eff,A}$  and the source terms due to transport across the phase interface  $\Gamma^A$ , which  
 161 are described in the following.

162 Mass transfer through an element of the interface between gas and liquid is driven by the  
 163 difference between the concentration  $Y^{A*}$  right at the interface, where both phases are  
 164 assumed to be in equilibrium, and the concentration  $Y^A$  in the bulk of each phase. Frequently,  
 165 the difference is small in the gas phase resulting in the one-sided model sketched in Figure 2.  
 166 The mass transfer coefficient  $k_L$  is defined as the constant of proportionality between the  
 167 mass flux  $G_L^A$  into the liquid and this concentration difference within the liquid, i.e.

$$G_L^A = k_L \rho_L (Y_L^{A*} - Y_L^A) . \quad (3)$$

168  $k_L$  depends on details of the mass transport from the interface through the liquid boundary  
 169 layer to the bulk within the liquid phase, which generally may comprise diffusive and  
 170 convective contributions as well as turbulence effects. For a bubble, the overall mas transfer  
 171 coefficient is obtained by summing the contributions from each interface element to give the  
 172 mass flux through the entire bubble surface. It thus becomes a function of the bubble shape  
 173 and the flow around it, both of which are determined by the bubble size, its velocity relative  
 174 to the liquid and material parameters. Among the latter, the diffusivity appears directly in the  
 175 mass transport problem, while viscosity and surface tension come into play indirectly by  
 176 affecting the flow field.



177

178 Figure 2: Simplified sketch of concentrations driving mass transfer across an interface.

179

180 The volumetric source term  $\Gamma_L^A$  is obtained from the mass flux  $G_L^A$  by multiplying with the  
 181 interfacial area concentration  $a_I$ . Furthermore, concentrations in the gas and liquid at the  
 182 interface are related by Henry's law with the constant denoted as  $He^A$ . Thus one obtains

$$\Gamma_L^A = k_L a_I \rho_L \left( He^A Y_G^A \frac{\rho_G}{\rho_L} - Y_L^A \right). \quad (4)$$

183 For the liquid side mass transfer coefficient  $k_L$  three correlations are considered which are  
 184 expressed in terms of dimensionless variables, namely Sherwood number  $Sh = k_L d_B / D_L^A$ ,  
 185 Reynolds number  $Re = |\mathbf{u}_G - \mathbf{u}_L| d_B \rho_L / \mu_L$ , and Schmidt number  $Sc = \mu_L / (\rho_L D_L^A)$ . A  
 186 comparison of all three correlations as function of  $Re$  is shown in the bottom part of Figure 3  
 187 below.

188 The first one,

$$Sh = \left( 2 + \frac{0.651 (Re Sc)^{1.72}}{1 + (Re Sc)^{1.22}} \right) \left( (1 + 0.433 Re^2)^{-1} + 4.23 \right)^{-0.055}, \quad (5)$$

189 was used in the simulations of Ayed et al. (2007) with reference to Mewes and Wiemann  
 190 (2003), who in turn quote it as a result for spherical bubbles from Brauer (1981). This latter  
 191 reference is obviously erroneous and should likely have been Brauer (1979) as also given by  
 192 Ayed et al. (2007). Upon close inspection however, the expression for the last factor in Eq.  
 193 (5) does not appear in Brauer (1979). Instead, a graphical result is displayed, from which a  
 194 number of data points are shown in the top part of Figure 3 (crosses). As may be seen, these  
 195 are very different from the expression given by Mewes and Wiemann (2003) (dotted line).  
 196 Hence, the origin and meaning of Eq. (5) is somewhat unclear.

197 Therefore, a fit formula to the graphical result from Brauer (1979) was developed (solid line  
 198 in the top part of in Figure 3) and is used in a second correlation for the mass transfer  
 199 coefficient, namely

$$Sh = \left( 2 + \frac{0.651 (Re Sc)^{1.72}}{1 + (Re Sc)^{1.22}} \right) \left( 1 + \frac{0.037 Re^{0.9}}{1 + 0.05 Re^{0.9}} \right). \quad (6)$$



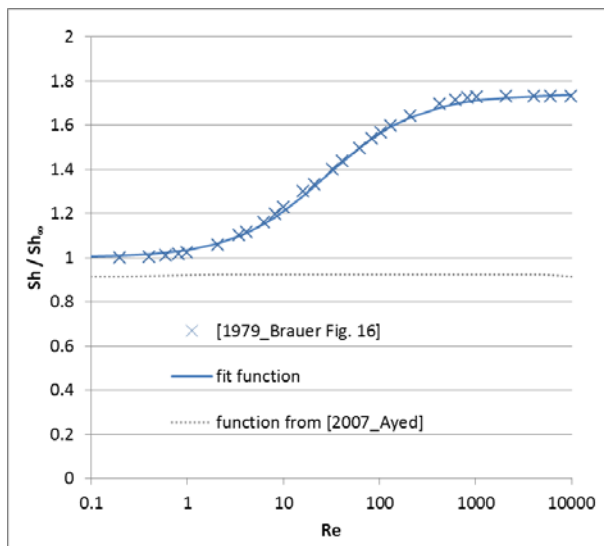
200 The results for spherical bubbles from Brauer (1979) on which Eq. (6) is based were  
 201 obtained by direct numerical simulations of the coupled equations for fluid dynamics and  
 202 mass transfer. Surfactants were not included in the simulations, hence it corresponds to an  
 203 absolutely clean bubble with a fully mobile interface. Conditions imposed at the bubble  
 204 surface were a free slip condition for the fluid dynamical part and a fixed concentration for  
 205 the mass transfer part. Accordingly, the internal circulation and the gas side resistance to  
 206 mass transfer are neglected. Both of these assumptions are typically made for gas bubbles  
 207 since the viscosity and diffusivity in the gas are much smaller than those in the liquid. The  
 208 motion of the interface relative to the liquid is of course determined by the imposition of the  
 209 spherical bubble shape, but within this assumption the development of the boundary layer  
 210 from the stagnation point at the bubble front to detachment and wake formation and the  
 211 rear end of the bubble are captured by the simulations.

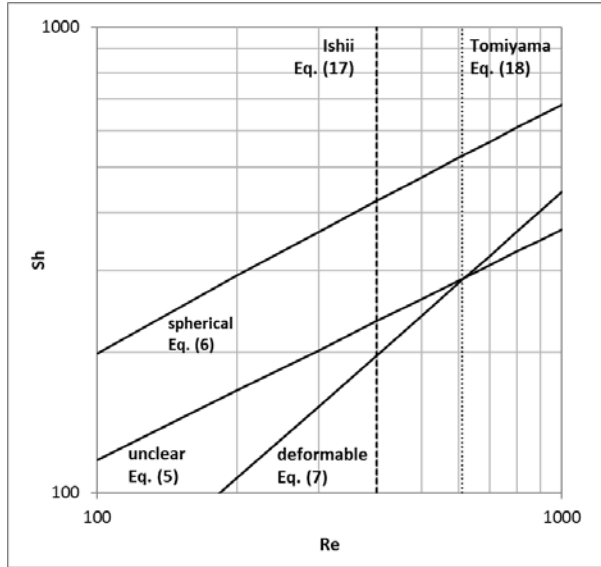
212 Finally, a third correlation is considered that applies for deformed bubbles, i.e.

$$Sh = (2 + 0.015 Re^{0.89} Sc^{0.7}). \quad (7)$$

213 This also appeared in Brauer (1979) and was quoted by Mewes and Wiemann (2003). In  
 214 addition it was compared with recent measurements on single bubbles (Merker et al. 2017)  
 215 and applied in a number of other simulations including mass transfer (e.g. Krauß and Rzehak,  
 216 2018 and references therein). The correlation Eq. 7 was proposed by Brauer (1979) based on  
 217 a review of experimental studies at varying  $Re$  and  $Sc$ . Unfortunately the water quality was  
 218 not reported, so the interface mobility is not known with certainty. While the internal  
 219 circulation and gas side resistance to mass transfer are included in principle, they are still  
 220 small effects for the reasons mentioned above. The dominant effect distinguishing this model  
 221 from the previous one is that the bubble shape and wobbling and their influence on the  
 222 boundary layer development and wake formation are captured.

223





224 Figure 3: Comparison of mass transfer correlations. Top part: the last factor in the correlation  
 225 from Mewes and Wiemann (2003), Eq. (5), (dotted line) is compared to the second factor in  
 226 the correlation from Brauer (1979), Eq. (6), (crosses: scanned from the graphical result in the  
 227 original work; solid line: fit formula used herein). Bottom part: the dependence of  $Sh$  on  $Re$   
 228 for  $Sc = 371$  corresponding to  $O_2$  in water at  $25^\circ C$  according to the correlations discussed in  
 229 section 3.3 is compared for the correlations from Eqs. (5) to (7). Also indicated are the values  
 230 of  $Re$  obtained for the terminal velocities for the two drag laws considered (see section 3.2).

231 The interfacial area concentration  $a_l$  in Eq. (4) is expressed as

$$a_l = \frac{6\alpha_G}{d_B} \quad (8)$$

232 by assuming spherical bubbles.

233 The Henry constant  $He^A$ , the molecular diffusion coefficient  $D_L^A$ , liquid density  $\rho_L$  and  
 234 viscosity  $\mu_L$  as well as the gas density  $\rho_G$  are obtained from the material model (see section  
 235 3.3) by inserting the appropriate values for the local temperature and pressure. The bubble  
 236 size  $d_B$  is taken as a constant in accordance with the experiments as discussed in section 2.

237

238 The effective diffusion coefficients  $D^{eff,A}$  consist of two contributions, a molecular one  $D^A$   
 239 and a turbulent one  $D^{turb,A}$ . The latter is typically dominant in the continuous liquid phase  
 240 and calculated from the simple but frequently used assumption of unity Schmidt number (e.g.  
 241 Cockx et al. 2001), i.e. from

$$Sc_L^{turb} = \frac{v_L^{turb}}{D_L^{turb,A}} = 1. \quad (9)$$

242 Herein, the turbulent kinematic viscosity  $v_L^{turb}$  is obtained from the turbulence model (see  
 243 section 3.2). No diffusive transport occurs between bubbles in the dispersed gas phase, i.e.  
 244  $D_G^{eff,A} = 0$ .

245 Boundary conditions required to obtain a unique solution of Eqs. (1) and (2) are a specified  
246 value of the mass fraction at an inlet, a vanishing normal derivative at an outlet, and  $Y_G^A =$   
247  $Y_L^A = 0$  on impermeable walls.  
248

249 3.2 Fluid Dynamics

250 Fluid dynamic phenomena are described by balance equations for mass and momentum in  
 251 each phase, which are summarized as follows. The continuity equations for both phases are

$$\frac{\partial}{\partial t}(\alpha_G \rho_G) + \nabla \cdot (\alpha_G \rho_G \mathbf{u}_G) = \Gamma_G^A \quad (10)$$

$$\frac{\partial}{\partial t}(\alpha_L \rho_L) + \nabla \cdot (\alpha_L \rho_L \mathbf{u}_L) = \Gamma_L^A, \quad (11)$$

252 and the momentum equations read

$$\begin{aligned} \frac{\partial}{\partial t}(\alpha_G \rho_G \mathbf{u}_G) + \nabla \cdot (\alpha_G \rho_G \mathbf{u}_G \otimes \mathbf{u}_G) \\ = -\alpha_G \nabla p_G + \nabla \cdot (\alpha_G \mathbf{T}_G) + \alpha_G \rho_G \mathbf{g} + \mathbf{F}_G^{inter} + \Phi_G^A \end{aligned} \quad (12)$$

$$\begin{aligned} \frac{\partial}{\partial t}(\alpha_L \rho_L \mathbf{u}_L) + \nabla \cdot (\alpha_L \rho_L \mathbf{u}_L \otimes \mathbf{u}_L) \\ = -\alpha_L \nabla p_L + \nabla \cdot (\alpha_L \mathbf{T}_L) + \alpha_L \rho_L \mathbf{g} + \mathbf{F}_L^{inter} + \Phi_L^A. \end{aligned} \quad (13)$$

253 Details on the derivation of these equations are available in several monographs (e.g. Drew  
 254 and Passman 1998, Yeoh and Tu 2010, Ishii and Hibiki 2011).

255 The last terms on the right in in Eqs. (12) and (13) represent sources due to the mass  
 256 transfer. The mass sources  $\Gamma^A$  are the same as already discussed in section 3.1. The so-called  
 257 secondary momentum sources  $\Phi^A$  represent the momentum carried along by the transferred  
 258 mass. A physical model for these sources consistent with all other aspects of the overall model  
 259 is given by

$$\Phi_G^A = -\max(0, \Gamma_L^A) \mathbf{u}_G - \min(0, \Gamma_L^A) \mathbf{u}_L \quad (14)$$

$$\Phi_L^A = \max(0, \Gamma_L^A) \mathbf{u}_G + \min(0, \Gamma_L^A) \mathbf{u}_L. \quad (15)$$

260 Since for the present application only a small amount of mass is transferred between the  
 261 phases, their magnitude is likewise small, but they are nonetheless included for the sake of  
 262 completeness.

263 The stress tensor is given by

$$\mathbf{T} = \mu^{eff} (\nabla \mathbf{u} + (\nabla \mathbf{u})^T), \quad (16)$$

264 where the effective dynamic viscosity  $\mu^{eff}$  comprises a viscous and a turbulent contribution.  
 265 For the liquid phase, the latter is calculated based on a k- $\omega$  SST model (Menter 2009).  
 266 According to the baseline model applied here, source terms are added to the base model,  
 267 which account for the bubble- induced turbulence (e.g. Rzehak and Krepper 2013a, Rzehak  
 268 and Kriebitzsch 2015, Ziegenhein et al. 2017, Parekh and Rzehak 2018). For the gas phase,  
 269 turbulence may be neglected because of the low gas density and the small spatial scales  
 270 imposed by the bubble size, i.e.  $\mu_G^{eff} = 0$ .

271 The primary momentum sources  $\mathbf{F}^{inter}$  represent the direct transfer of momentum across  
 272 the interface and are related as  $\mathbf{F}_G^{inter} = -\mathbf{F}_L^{inter}$  to satisfy momentum conservation. They  
 273 comprise several different contributions and the closure relation used for each of these  
 274 according to the applied baseline model is shown in Table 2 (e.g. Ziegenhein et al. 2013,  
 275 Rzehak et al. 2015, Rzehak and Krepper 2015, or Rzehak et al. 2017a). The drag force

276 correlation of Ishii and Zuber (1979) used in the original baseline model corresponds to a  
 277 contaminated water quality. In addition, a correlation proposed by Tomiyama et al. (1998) for  
 278 clean water is considered. To be definite, the correlation of Ishii and Zuber (1979) reads

$$C_D = \max\left(\frac{24}{Re}(1 + 0.1 Re^{0.75}), \min\left(\frac{2}{3}\sqrt{Eo}, \frac{8}{3}\right)\right), \quad (17)$$

279 while that of Tomiyama et al. (1998) is given by

$$C_D = \max\left(\min\left(\frac{16}{Re}(1 + 0.15 Re^{0.687}), \frac{48}{Re}\right), \frac{8}{3} \frac{Eo}{Eo + 4}\right). \quad (18)$$

280 Two further relations are required to complete the above system of equations. With the  
 281 assumption that each phase is incompressible, these are provided by conservation of volume,  
 282 expressed as  $\alpha_G + \alpha_L = 1$ , and equilibrium of pressures, expressed as  $p_G = p_L = p$ .

283 Boundary conditions on solid walls are no-slip for the liquid and free slip for gas phase. The latter  
 284 assumes that direct contacts between the bubbles and the walls can be neglected. The need  
 285 to resolve the viscous boundary layer is avoided by applying a single phase turbulent wall  
 286 function. At an inlet, profiles for the gas fraction and gas and liquid velocities are prescribed.  
 287 Pressure is imposed as an outlet condition together with vanishing tangential velocity  
 288 components and a vanishing normal derivative of gas fraction.

289 Table 2: Summary of bubble force correlations.

force	reference
drag (contaminated condition)	Ishii and Zuber (1979)
drag (clean condition)	Tomiyama et al. (1998)
shear lift	Tomiyama et al. (2002)
wall lift	Hosokawa et al. (2002)
turbulent dispersion	Burns et al. (2004)
virtual mass	constant coefficient $C_{VM} = \frac{1}{2}$

290

291

292

293 3.3 Material Properties

294 The present section summarizes correlations assembled from the literature to model the  
 295 temperature dependence of solubility and diffusivity of O<sub>2</sub> in water, surface tension between  
 296 O<sub>2</sub> and water as well as viscosity and density of water and gaseous O<sub>2</sub>. All correlations are  
 297 valid at atmospheric pressure.

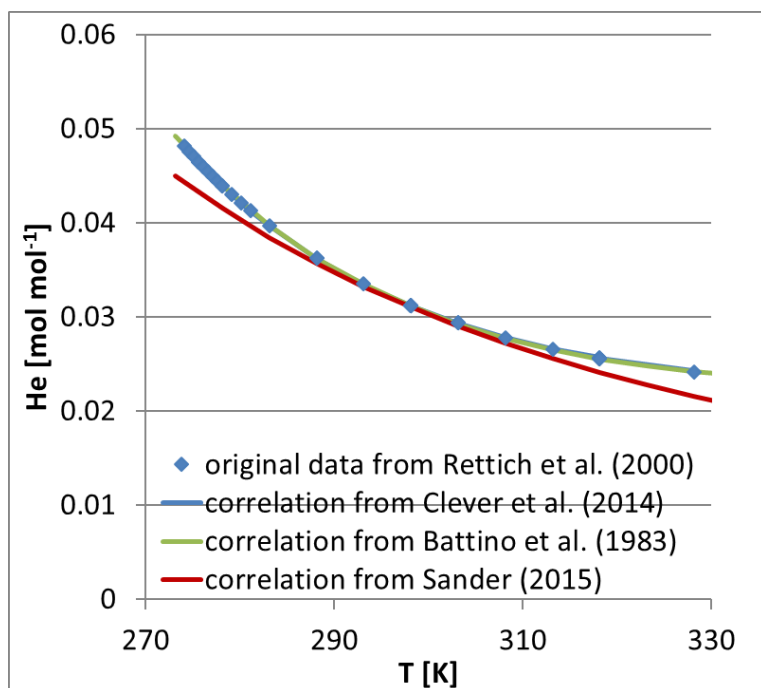
298 3.3.1 Solubility

299 The solubility of O<sub>2</sub> in water is quite well studied. A rather recent compilation of data and  
 300 assessment of correlations for the Henry constant is given in Clever et al. (2014). In this  
 301 review, the most precise measurements are attributed to Rettich et al. (2000). These are  
 302 shown in Figure 4 together with a correlation based on the recommended one from Clever et  
 303 al. (2014). Since the results of Clever et al. (2014) and Rettich et al. (2000) were expressed in  
 304 units of 1/Pa rather than mol/mol as desired here, these results were multiplied by  
 305  $\rho^{H_2O} / M^{H_2O}$  where  $\rho^{H_2O}$  was determined in accordance with Rettich et al. (2000) from a  
 306 correlation due to Kell (1975) and  $M^{H_2O} = 0.018 \text{ kg/mol}$ . Then the fit coefficients were  
 307 adjusted to get the desired result in a single pass as

$$He = R T \exp\left(-4.072752 - \frac{5756.888 [K]}{T} + \frac{1075294 [K^2]}{T^2}\right) \cdot \left[\frac{mol}{J}\right]. \quad (19)$$

308 It may be noted that a three-parameter fit formula of different form proposed in the earlier  
 309 review of Battino et al. (1983) yields numerically the same results. A simpler two-parameter  
 310 fit due to Sander (2015) applies only to a more limited range around room temperature.

311



312

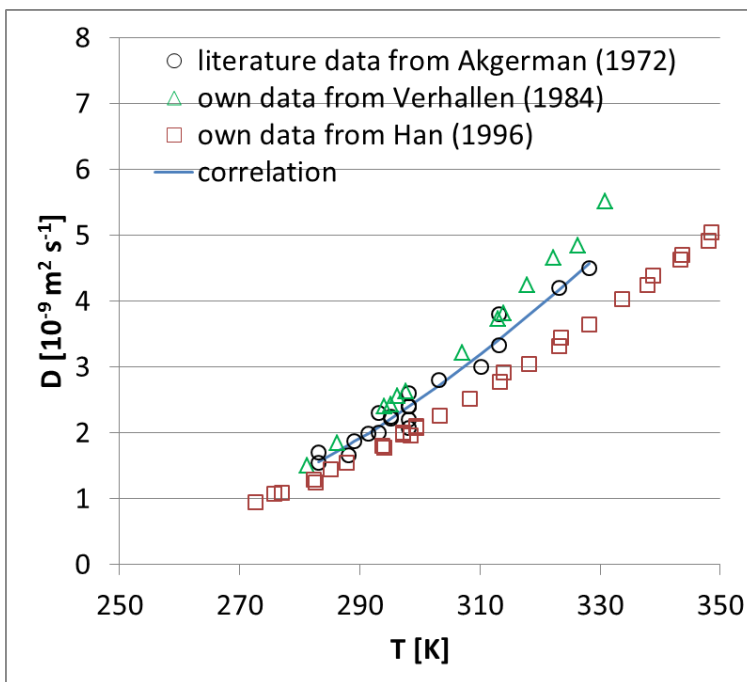
313 Figure 4: Henry constant for O<sub>2</sub> in water.

314 3.3.2 Diffusivity

315 As shown in Figure 5, data on the diffusivity of O<sub>2</sub> in water found in the literature (Akgerman  
 316 and Gainer 1972, Verhallen et al. 1984, Han and Bartels 1996) exhibit a rather large spread in  
 317 particular at elevated temperatures. Since a detailed assessment of the accuracy of the  
 318 different measurements is not possible here, we have chosen the older but more frequently  
 319 relied on data compiled by Akgerman and Gainer (1972) which comprise results from the  
 320 earlier works of Himmelblau (1964), Ferrell and Himmelblau (1967), Wise and Houghton  
 321 (1966) and a few smaller studies. These data are fitted by correlation

$$D_L^{O_2} = \exp\left(1.228 + \frac{2100 [K]}{T} - \frac{657600 [K^2]}{T^2}\right) \cdot 10^{-9} \left[\frac{m^2}{s}\right]. \quad (20)$$

322



323

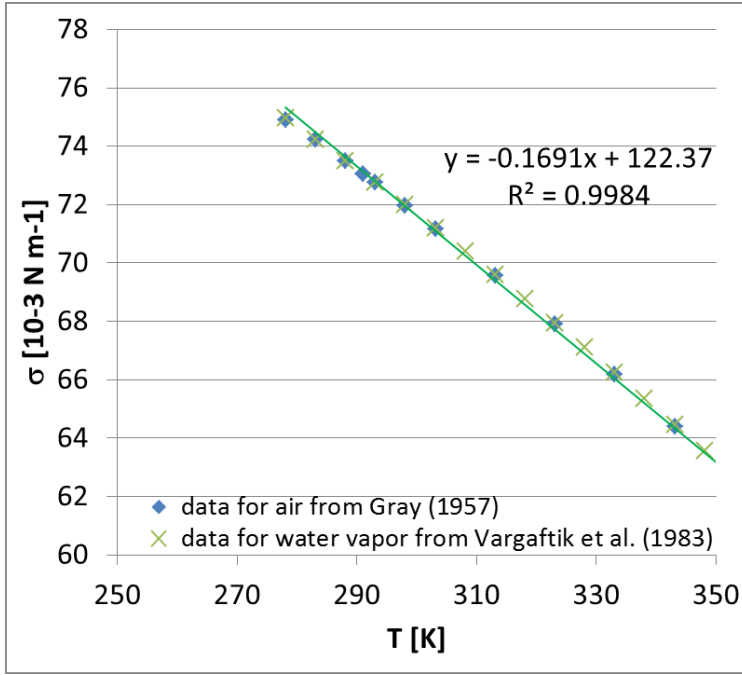
324 Figure 5: Diffusivity of O<sub>2</sub> in water.

325 3.3.3 Surface Tension

326 Data on the surface tension between mutually saturated mixtures of O<sub>2</sub> and water could not  
 327 be found in the literature. However, for non-adsorbing gases the surface tension to the same  
 328 liquid is typically the same. Therefore, we here substitute the surface tension for water with  
 329 its own vapor which is quite well characterized (Vargaftik et al. 1983). From Figure 6, it is seen  
 330 that these data are undistinguishable from data on air in contact with water (Gray, 1957, sect.  
 331 2p-2). In a range of temperatures around ambient conditions these data are well represented  
 332 by a linear temperature dependence

$$\sigma = \left(122.37 - 0.1691 \frac{T}{[K]}\right) \cdot 10^{-3} \left[\frac{N}{m}\right], \quad (21)$$

333 which is also shown in Figure 6.



334

335 Figure 6: Surface tension of gases in water.

336 3.3.4 Viscosity

337 In the dilute limit, the presence of O<sub>2</sub> in the liquid phase may be neglected. For the viscosity  
 338 of pure water a highly accurate description valid over a very large range of conditions is  
 339 available (Huber et al. 2009) which is adopted by the IAPWS. However, sometimes a simpler  
 340 correlation with a smaller range of applicability is advantageous to work with. To this end the  
 341 Vogel-Fulcher-Tammann type formula

$$\mu_L^{H_2O} = \exp\left(3.184 + \frac{570.6[K]}{T - 140[K]}\right) \cdot 10^{-6}[Pa s] \quad (22)$$

342 has been shown to provide a good description in the range from 5 ... 95 °C (Rzehak and  
 343 Krepper 2016).

344 For the gas phase Sutherland's formula is applied (e.g. Chapman and Cowling 1970, sect.  
 345 12.32), i.e.

$$\mu_G = \mu_{ref} \left(\frac{T}{T_{ref}}\right)^{3/2} \frac{T_{ref} + T_S}{T + T_S}, \quad (23)$$

346 where  $\mu_{ref}$  is the viscosity at the reference temperature  $T_{ref}$  and  $T_S$  is a material dependent  
 347 constant. The parameters for O<sub>2</sub> and air are summarized in Table 3.

348

gas	$T_S$ [K]	$T_0$ [K]	$\mu_0$ [ $10^{-6} Pa s$ ]
O <sub>2</sub>	127	292.25	20.18

349

350 Table 3: Parameters for Sutherland correlation Eq. (23).

351



352 3.3.5 Density

353 Similarly, for the density of pure water the most accurate and complete description adopted  
354 by the IAPWS is given in Wagner and Pruß (2002). A simpler and more easily applicable  
355 quadratic fit formula

$$\rho_L^{H_2O} = \left( -0.0035 \left( \frac{T}{[K]} \right)^2 + 1.824 \frac{T}{[K]} + 763.42 \right) \cdot \left[ \frac{kg}{m^3} \right], \quad (24)$$

356 can be applied in the range from 5 ... 95 °C (Rzehak and Krepper 2016).

357 The gas phase is modeled as an ideal gas or an ideal mixture thereof, i.e. the gas density given  
358 by

$$\rho_G = \frac{p M_G}{R T}, \quad (25)$$

359 where  $M^{O_2} = 32.0 \text{ kg / kmol}$  is the molar mass of O<sub>2</sub> and  $R$  is the universal gas constant.  
360 The pressure in Eq. (25) is the local fluid pressure, which varies over the height of the fluid  
361 domain mainly due to hydrostatics. As it will turn out this variation has a significant influence  
362 on the equilibrium at the interface. In principle a Laplace pressure of  $4 \sigma / d_B$  should also be  
363 included, but this term is negligibly small for the present applications.  
364

365 4 SIMULATION RESULTS

366 To perform the simulations the commercial software ANSYS CFX 17.2 is used. Due to a lack of  
 367 symmetry in the geometry and boundary conditions, a fully three-dimensional simulation is  
 368 run. A grid spacing of 5 mm in the lateral directions and stretched by a factor of 6 in the axial  
 369 direction was determined to provide a reasonably well converged solution in a grid  
 370 independency study. Concentrations, phase fractions, and phasic velocities at the two inlets  
 371 are set according to the experimental description given in Section 2. For the turbulence,  
 372 generic values of intensity (5%) and viscosity ratio (10) are imposed. Uniform distributions of  
 373 all of these quantities over each inlet are assumed. Pressure at the outlet is set to atmospheric  
 374 pressure unless stated otherwise. This corresponds to neglecting the hydrostatic head of the  
 375 water in the reservoir above the test section. Based on the measurements dicussed in Section  
 376 2, the bubble size distribution may be taken as monodisperse with a constant bubble size. The  
 377 experimentally determined mean value of  $d_B = 1.8$  mm is used. Material properties according  
 378 to the correlations of section 3.3 are evaluated at a temperature of 25 °C and the local  
 379 pressure. In the course of the investigation, several model variants are considered, which are  
 380 summarized in Table 4 for convenience. More detailed explanations are provided in the text.  
 381

designation	drag force model	mass transfer coefficient model	pressure
ShConst-CdTomi	Eq. (18)	$Sh = 400$	reservoir empty
ShConst-CdIshii	Eq. (17)	$Sh = 330$	reservoir empty
ShZero-CdTomi	Eq. (18)	$Sh = 0$	reservoir empty
ShZero-CdIshii	Eq. (17)	$Sh = 0$	reservoir empty
ShDef-CdTomi	Eq. (18)	Eq. (7)	reservoir empty
ShSph-CdIshii	Eq. (17)	Eq. (5)	reservoir empty
ShXxx-CdIshii	Eq. (17)	Eq. (6)	reservoir empty
ShDef-CdTomi-pressure	Eq. (18)	Eq. (7)	reservoir full
ShXxx-CdIshii-pressure	Eq. (17)	Eq. (6)	reservoir full

382  
 383 Table 4: Summary of investigated model variants.

384  
 385

386 4.1 Fluid Dynamics

387 Turning first to the fluid dynamics, results from experiment (symbols) and simulations (lines)  
 388 are displayed in Figure 7 and Figure 8. Lateral profiles of gas fraction, liquid velocity and  
 389 turbulent kinetic energy, as well as relative velocity between liquid and gas are shown at  
 390 different locations along the test section. Since in the experiments only liquid velocity  
 391 fluctuations in the axial direction have been recorded, isotropy is assumed like in Ayed et al.  
 392 (2007) to express the turbulent kinetic energy as  $\kappa_L = 3u_L'^2/2$ . In the simulations, the two  
 393 models for the drag force described in section 3.2 are compared, one being valid for  
 394 contaminated interfaces (thick lines, labeled “Ishii”) while the other one was proposed for  
 395 clean interfaces (thin lines, labeled “Tomi”). Each of these models is combined with two  
 396 prescriptions for the mass transfer, which has either been negelcted (solid lines labeled

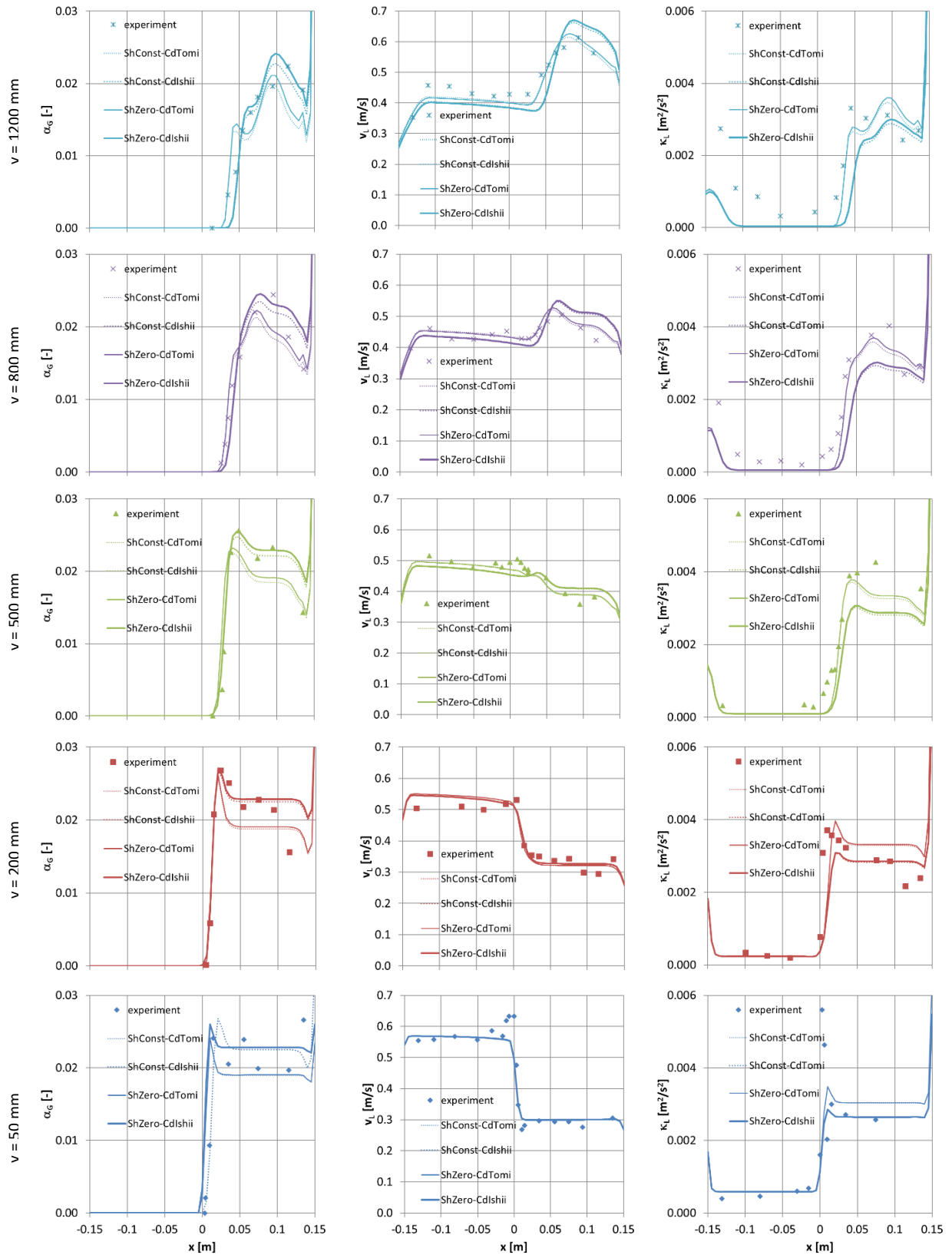
397 “ShZero”) or set to an adjusted value as described further below in section 4.2 (dotted lines  
398 labeled “ShConst”).

399 From the comparison of the two mass transfer prescriptions it is seen that for the present  
400 case, where the bubble size remains unaffected and the only action of the mass transfer on  
401 the fluid dynamics comes from the secondary momentum sources in Eqs. (14) and (15),  
402 there is only a minor effect. This influence of the mass transfer is most visible in the gas  
403 fractions at the highest level, but even there it is much smaller than that of the different drag  
404 forces. Otherwise, the effect is sometimes hardly discerned at all. Hence, this may be termed  
405 a one-way-coupling situation, in which the fluid dynamics of course affects the mass transfer,  
406 but not vice versa.

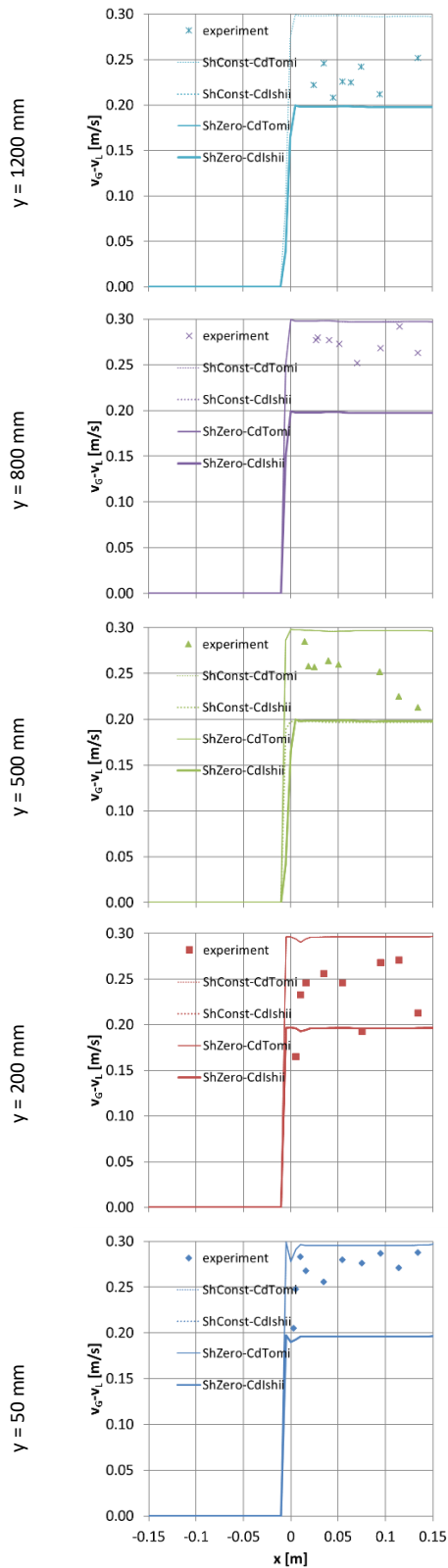
407 Looking in more detail at the flow development, it can be seen in qualitative terms that the  
408 liquid velocities on both sides, left without and right with gas injection, tend to equalize up to  
409 a height of around 500 mm. This would be expected also for a single phase flow due to the  
410 action of viscosity. In the present multiphase flow, the liquid on the right with gas injection is  
411 further accelerated due to momentum transfer from the buoyant gas. Therefore, from around  
412 800 mm height on, the liquid velocity on the right exceeds that on the left side. Near the inlet,  
413 the gas content is distributed almost uniformly over the cross section of the right side of the  
414 channel, where the injection takes place. The left side of the channel remains free of gas over  
415 the entire height where measurements are taken. In fact, with increasing height the gas is  
416 continually shifted away from the channel center and towards the right wall. This can be  
417 attributed to the action of the lift force. The level of turbulence is significantly higher on the  
418 right side of the channel (where gas is injected) than on the left side of the channel (without  
419 gas injection) at all height levels. This is a clear signature of the bubble-induced turbulence.  
420 At the lower heights a peak in the turbulent kinetic energy is seen at the position of the splitter  
421 plate separating the two inlet regions which is caused by the strong shear gradient at this  
422 position. Also caused by shear turbulence is the peak developing with increasing height near  
423 the left wall of the channel where no gas is present.

424 Quantitatively, differences between the two drag models are most pronounced for the  
425 relative velocity between gas and liquid phase shown in Figure 8, hence these are discussed  
426 first. As is well known, the rise velocity is higher for clean bubbles than for contaminated ones  
427 which is also seen in the simulations. In comparison with the experimental data (symbols),  
428 the measurements are closer to the calculations for the clean case (thin lines) at the lowest  
429 level and closer to the calculations for the contaminated case (thick lines) at the highest level.  
430 This suggests the possibility that the bubbles are clean when they are injected in the system  
431 but collect contaminations during their rise. Taking into account the intermediate levels, this  
432 picture is not so clear anymore, hence it must be left as a hypothesis. It can be stated clearly  
433 however, that the calculations for clean and contaminated cases provide upper and lower  
434 bounds for the observed behavior.

435 Results for gas fraction, liquid velocity, and turbulent kinetic energy are collected in Figure 7.  
436 Smaller differences between the simulations based on the two drag models are seen which  
437 can be understood as consequences of the different relative velocities. A higher relative  
438 velocity of the bubbles tends to decrease the residence time of the bubbles which leads to a  
439 lower observed gas content. Hence, gas fractions calculated for the clean case (thin lines) tend



440 Figure 7: Comparison of experimental data (symbols) and simulation results (lines) using  
 441 several models as described in the text. Lateral profiles are shown at different locations in  
 442 the test section as indicated on the left of each row for gas fraction  $\alpha_G$  (left column),  
 443 liquid velocity  $v_L$  (middle column), and turbulent kinetic energy  $\kappa_L$  (right column).



444 Figure 8: Comparison of experimental data (symbols) and simulation results (lines) using  
 445 several models as described in the text. Lateral profiles are shown at different locations along  
 446 the test section as indicated on the left of each row for the relative velocity  $v_G - v_L$ .

447

448 to be lower than those calculated for the contaminated case (thick lines). Due to the higher  
449 gas content, a larger amount of momentum is transferred from the gas to the liquid phase  
450 which gives a higher liquid velocity in the right part of the test section where gas is present for  
451 the contaminated case than for the clean case. Likewise a higher turbulent kinetic energy  
452 might be expected since the contribution to the bubble-induced turbulence is proportional to  
453 the gas fraction. However, it is also proportional to the relative velocity which is higher for  
454 the clean than for the contaminated case. Of the two competing effects the latter is seen to  
455 dominate.

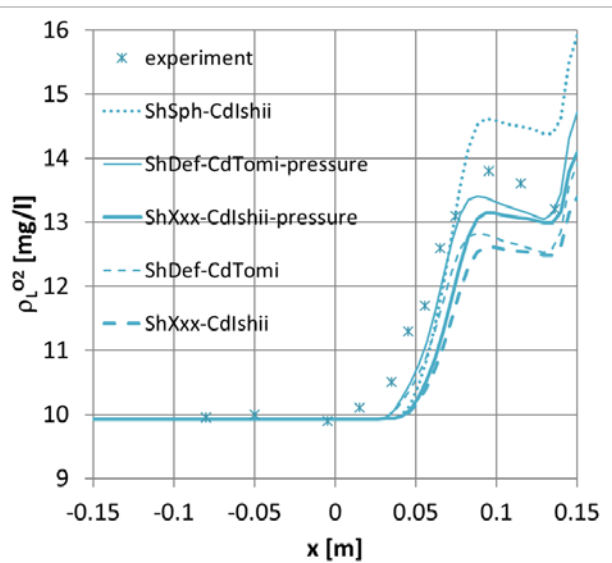
456 Overall agreement between simulation results (lines) and experimental data (symbols) is  
457 quite good for both drag force models. The model of Ishii and Zuber (1979) for contaminated  
458 interfaces comes a bit closer to the measurements for the gas fraction while the model of  
459 Tomiyama et al. (1998) for clean interfaces matches the liquid velocity and turbulent kinetic  
460 energy a bit better. The peak in turbulent kinetic energy seen in the experiment for the lowest  
461 height levels at the location of the splitter plate is significantly underestimated in the  
462 simulations. The same holds for the peak near the left channel wall that becomes most  
463 prominent at the highest levels. Both of these are likely due to shortcomings of the shear-  
464 induced turbulence modeling by the  $k-\omega$  SST model. In addition, the simulations show  
465 pronounced peaks in gas fraction and turbulent kinetic energy near the right channel wall.  
466 Since these are below the spatial resolution of the measurements, their significance remains  
467 open.

## 468 4.2 Mass Transfer

469 Concerning mass transfer several different model variants are compared. In addition to the  
470 choice of the model for the mass transfer coefficient (see Eqs. (5) to (7)) simulation results  
471 for the mass transfer also depend on the drag model, because this determines the bubble  
472 Reynolds-number. To keep the number of different variants tractable, the Ishii-Zuber drag  
473 model for contaminated bubbles is combined with the mass transfer coefficient models of Eqs.  
474 (5) (designated as Sh<sub>Xxx</sub>-Cd<sub>Ishii</sub>) and (6) (designated as Sh<sub>Sph</sub>-Cd<sub>Ishii</sub>) for spherical bubbles,  
475 since the shape of contaminated bubbles is closer to spherical. For deformable clean bubbles  
476 the Tomiyama drag model is combined with the mass transfer coefficient models of Eqs. (7)  
477 (designated as Sh<sub>Def</sub>-Cd<sub>Tomi</sub>). A further significant dependence is found on the pressure,  
478 which in the experiment depends on the water level in the reservoir above the test section.  
479 This effect is caused by a corresponding change in the gas density according to the ideal gas  
480 law Eq. (25), which in turn appears in the mass transfer source Eq. (4). To assess this effect,  
481 in addition to the standard setting corresponding to an empty reservoir, also the case of a  
482 completely filled reservoir is considered (the latter identified by appending -pressure to the  
483 designation).

484 A comparison of the above variants is made for the concentration profiles of O<sub>2</sub> in the liquid  
485 at the highest level in the test section, where the differences are most pronounced. From the  
486 results shown in Figure 9, it may be seen that no model variant gives an entirely satisfactory  
487 match with the measurements. With the imposed concentration at the inlet as the reference,  
488 the spherical model (Sh<sub>Sph</sub>-Cd<sub>Ishii</sub>) overpredicts the measured concentrations by ~20% while  
489 the deformable model (Sh<sub>Def</sub>-Cd<sub>Tomi</sub>) underpredicts them by a similar amount. The model  
490 of somewhat unclear origin (Sh<sub>Xxx</sub>-Cd<sub>Ishii</sub>), although described as applying to spherical  
491 bubbles by Mewes and Wiemann (2003) gives more similar results as the one for deformable

492 bubbles. Differences arising from the drag model appear small compared to differences  
 493 arising from the mass transfer model. The effect of an increased pressure due the condition  
 494 of a filled reservoir at the top of the test section (ShDef-CdTomi-pressure and ShXxx-CdIshii-  
 495 pressure) is to increase the concentration cutting the difference to the measurement in half.



496

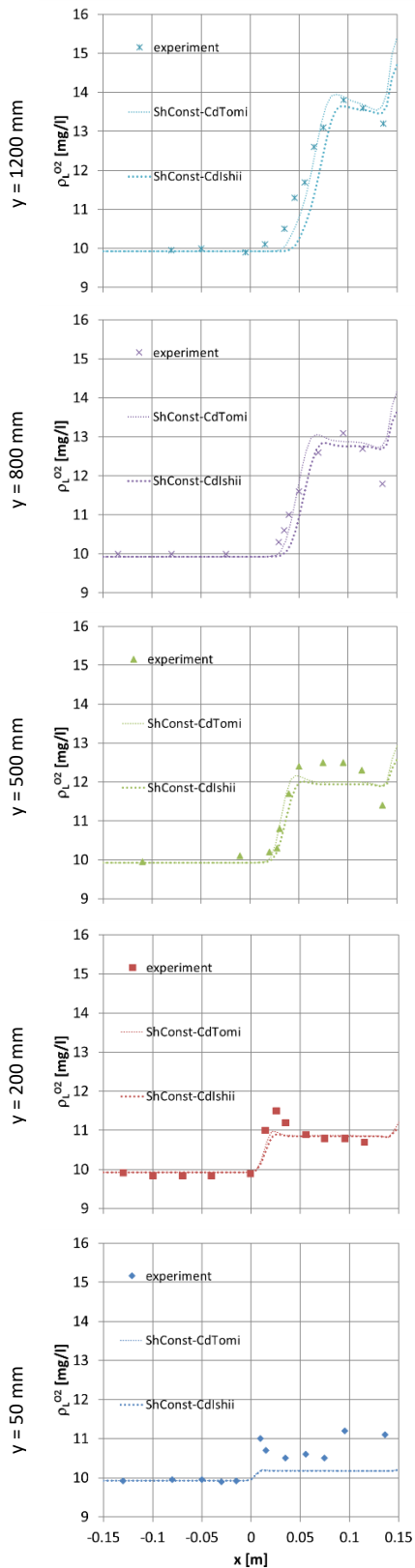
497 Figure 9: Comparison of experimental data (symbols) and simulation results (lines) using  
 498 several models as described in the text. Lateral profiles are shown at highest level of the test  
 499 section ( $y = 1200$  mm) for the mass concentration of oxygen in the liquid  $\rho_L^{O_2}$ .

500

501 It is clear from the definitions in section 3.1 that the mass transfer coefficient does not vary  
 502 throughout the flow domain. Thus, each mass transfer correlation only picks a constant value  
 503 according to the overall flow parameters. In order to see how the development of the  
 504 concentration profiles within the flow domain can be represented in the simulations, an  
 505 adjusted value of the mass transfer coefficient has been determined that matches the data  
 506 at the highest level (designated as ShConst). Values providing the best match are  $Sh = 330$  for  
 507 the Ishii-Zuber drag law and  $Sh = 400$  for the Tomiyama drag law.

508 These results are shown in Figure 10. As may be expected, the concentration of oxygen in the  
 509 liquid phase increases with increasing height. The shape of the concentration profiles follows  
 510 the distribution of the gas fraction rather closely. In the left part of the channel, where no gas  
 511 is injected, the concentration stays at its inlet value over the entire height where  
 512 measurements are taken. With the adjustment at the highest level, the overall agreement  
 513 between simulated (lines) and measured (symbols) concentrations of  $O_2$  at the lower levels is  
 514 quite good. Only at the lowest level ( $y = 50$  mm) the measured data are significantly  
 515 underpredicted. Concerning the shape of the concentration profiles, the step between the  
 516 two streams of the mixing layer is captured rather well. However, the dip at the nearest  
 517 measurement point to the wall is not reproduced by the simulations. Still closer to the wall  
 518 the simulations results show a steep increase similar as already observed for the gas fractions.  
 519 Differences between the two drag models are found to be only small.

520



521 Figure 10: Comparison of experimental data (symbols) and simulation results (lines) using  
 522 several models as described in the text. Lateral profiles are shown at different locations along  
 523 the test section as indicated on the left of each row for the mass concentration of oxygen in  
 524 the liquid  $\rho_L^{O_2}$ .



## 525 5 DISCUSSION AND CONCLUSIONS

526 Concerning fluid dynamics, quite good agreement was found for all of the measured  
527 quantities, namely gas fraction, mean liquid velocity, liquid turbulent kinetic energy, and  
528 relative velocity between the phases. The biggest uncertainty comes from the unknown water  
529 quality which has a significant impact on the relative velocity, that in turn affects all other  
530 fluid dynamic aspects as well as the mass transfer. In the present work, two different drag  
531 models from Ishii and Zuber (1979) and Tomiyama et al. (1998) corresponding to  
532 contaminated and clean conditions, respectively, were applied. Simulation results from these  
533 two models bracket the measured relative velocities and give approximate bounds for the  
534 other observables. Since water quality is difficult to control in practical applications this  
535 finding is quite useful. Comparison at different positions along the test section indicates the  
536 possibility that clean conditions prevail at the inlet but contaminations are accumulated on  
537 the gas-liquid interfaces during the flow. A more precise analysis is impeded by superimposed  
538 statistical variations in the measured data. However, to capture such effects the commonly  
539 used model frameworks would need to be substantially augmented by equations describing  
540 the contaminant concentration in the bulk and at the interfaces as well as models for the  
541 adsorption process.

542 Concerning mass transfer, none of the simple but frequently used correlations for the mass  
543 transfer coefficient of single bubbles that were compared gave an entirely satisfactory  
544 agreement with the measured concentrations. Assuming the most favorable condition for the  
545 pressure, the model for deformable bubbles from Brauer (1979) and the model of somewhat  
546 unclear origin used by Ayed et al. (2007) come within reach of the measurements. Which drag  
547 law is used in conjunction with the mass transfer model appears to be of minor importance.  
548 However, due to the uncertainties involved and the restriction of the test case to only a single  
549 value of the bubble size a definite recommendation for their general use cannot yet be given.  
550 Hence, to obtain a general correlation for the mass transfer coefficient of single bubbles that  
551 applies in a wide range of relevant parameters including different regimes of bubble shape  
552 and dynamics further investigations are necessary. A related aspect of the overall model that  
553 should be considered further is a more refined model describing the turbulent diffusivity  
554 depending on the local flow conditions by additional model equations for the variance of  
555 concentration fluctuations and its dissipation rate, as considered e.g. by Zhang et al. (2018),  
556 rather than just using a constant turbulent Schmidt number. A final minor issue in this context  
557 that nonetheless deserves to be improved is a lack of precise data on the diffusivity of O<sub>2</sub> in  
558 water.

559 Comparison may also be made with the previous simulation model by Ayed et al. (2007). The  
560 main difference concerning the applied closures is that these authors use a more elaborate  
561 turbulence model that treats shear- and bubble-induced turbulence as separate fields, while  
562 in the present work no such distinction is made and a single field representing the sum of  
563 both is used. While the model of Ayed et al. (2007) is potentially more general, it also requires  
564 further assumptions to be introduced in order to model the coupling between the fields  
565 relating to which hardly any evidence is available. As the present results show, at least for the  
566 conditions investigated no benefit results from the more complex model.

567 Comparing the simulation results mostly similar observations are made. In particular, the  
568 peak near the right channel wall in the gas fraction, turbulent kinetic energy, and oxygen  
569 concentration is also found in the simulations of Ayed et al. (2007) although for the  
570 concentration it is of lower magnitude there. Likewise, the underprediction of the peak in

571 turbulent kinetic energy near the left channel wall also occurs in the simulations of Ayed et  
 572 al. (2007). However their simulations overpredict TKE peak at splitter plate for the second  
 573 height level, which is likely related to the different inlet conditions, which they took from the  
 574 measured profiles at the lowest lowest instead of constant generic values as used here. The  
 575 biggest difference is that in the simulations of Ayed et al. (2007) the transition between the  
 576 two streams occurs further towards the right channel wall for the turbulent kinetic energy as  
 577 well as for the gas fraction and oxygen concentration. In this regard the present simulations  
 578 are closer to the measured data. The difference can be traced to different profiles of turbulent  
 579 viscosity and thus ultimately to the different turbulence models that were used. On the other  
 580 hand, the overall concentration level in the right stream matches the measurements better  
 581 in their simulations than in the present ones. Both of these differences may in fact be related.  
 582 Overall, considering the difference in turbulence modeling which gives rise to different  
 583 turbulent viscosities and hence different distribution of gas, the agreement between the  
 584 simulations is as good as may be expected.

585 To support further model development for the mass transfer, better validation data are still  
 586 needed, which provide a parametric variation especially of the bubble size that figures as an  
 587 important parameter in the closure correlations. In this context, the present results show that  
 588 a precise knowledge of the pressure is required since this has a significant impact on the  
 589 equilibrium concentrations in gas and liquid. This is an issue that has not received due  
 590 attention in previous validation experiments. An accompanying measurement of pressure  
 591 within the test section can serve this purpose and is easily done. To the least a precise  
 592 specification where exactly the facility is open to the atmosphere must be provided such that  
 593 the hydrostatic pressure at any point in the system can be calculated. The effect of  
 594 temperature is relatively small since kinematic viscosity and diffusivity have a similar  
 595 temperature-dependence which gives only a weak influence on the Schmidt number. A  
 596 quantification of measurement errors would be very helpful in order to determine which part  
 597 of eventual deviations should be attributed to the simulation model.

598

599 6 ACKNOWLEDGEMENT

600 This work has been carried out in the frame of a research project (GZ: RZ 11/3-1) funded by  
 601 the DFG.

602

603 7 NOMENCLATURE

**Latin Formula Characters**

<b>Symbol</b>	<b>Description</b>	<b>Unit</b>	<b>Symbol</b>	<b>Description</b>	<b>Unit</b>
$a_i$	interfacial area concentration	$m^{-1}$	$R$	universal gas constant	$J K^{-1} mol^{-1}$
$c$	molar concentration	$mol m^{-3}$	$Re$	Reynolds number	-
$d_B$	bubble diameter	$m$	$Sc$	Schmidt number	-
$D$	lateral dimension	$m$	$Sh$	Sherwood number	-
$D$	diffusion coefficient	$m^2 s^{-1}$	$t$	time	$s$

$F$	force per unit volume	$\text{N m}^{-3}$	$T$	temperature	$^{\circ}\text{C}, \text{K}$
$g$	acceleration of gravity	$\text{m s}^{-2}$	$\mathbf{T}$	stress tensor	$\text{N m}^{-2}$
$G$	mass flux	$\text{kg m}^{-2} \text{s}^{-1}$	$\mathbf{u}$	mean velocity	$\text{m s}^{-1}$
$H$	axial dimension	$\text{m}$	$\mathbf{u}'$	fluctuating velocity	$\text{m s}^{-1}$
$He$	Henry constant	-	$W$	spanwise dimension	$\text{m}$
$J$	Superficial velocity = volumetric flux	$\text{m s}^{-1}$	$x$	lateral coordinate	$\text{m}$
$k$	mass transfer coefficient	$\text{m s}^{-1}$	$X$	mole fraction	-
$M$	molar mass	-	$y$	axial coordinate	$\text{m}$
$p$	pressure	$\text{Pa}$	$Y$	mass fraction	-
$r$	radial coordinate	$\text{m}$	$z$	spanwise coordinate	$\text{m}$

604

**Greek Formula Characters**

Symbol	Description	Unit	Symbol	Description	Unit
$\alpha$	phase fraction	-	$\nu$	kinematic viscosity	$\text{m}^2 \text{s}^{-1}$
$\epsilon$	turbulent dissipation rate	$\text{m}^2 \text{s}^{-3}$	$\rho$	density, mass concentration	$\text{kg m}^{-3}$
$\Gamma$	source term due to mass transfer	$\text{kg m}^{-3} \text{s}^{-1}$	$\sigma$	surface tension	$\text{N m}^{-1}$
$\kappa$	specific turbulent kinetic energy	$\text{m}^2 \text{s}^{-2}$	$\phi$	secondary momentum source due to mass transfer	$\text{N m}^{-3}$
$\mu$	dynamic viscosity	$\text{kg m}^{-1} \text{s}^{-1}$	$\omega$	turbulent frequency	$\text{s}^{-1}$

605

**Latin Indices**

Symbol	Description	Symbol	Description
$A$	of transferred species	$L$	liquid phase
$eff$	effective	$mol$	molecular
$G$	gas phase	$O_2$	of oxygen
$H_2O$	of water	$turb$	turbulent
$in1$	at inlet 1	$X$	of any species
$in2$	at inlet 2		

606

607

608 **8 REFERENCES**

609 Akgerman, A. and Gainer, J. L., 1972. Predicting gas-liquid diffusivities. *Journal of Chemical*  
610 *and Engineering Data* 17, 372–377.

611 Ayed, H., Chahed, J., and Roig, V., 2007. Hydrodynamics and mass transfer in a turbulent  
612 buoyant bubbly shear layer. *AIChE Journal* 53, 2742–2753.

613 Battino, R., Rettich, T. R. and Tominaga, T., 1983 The Solubility of Oxygen and Ozone in Liquids.  
614 *Journal of Physical and Chemical Reference Data* 12, 163-178.

615 Brauer, H., 1979. Particle / fluid transport processes. *Progress in Chemical Engineering* 17, 61-  
616 99.

617 Brauer, H., 1981. Mass transfer operations between liquid films and adjoining gas streams.  
618 *Progress in Chemical Engineering* 19, 81–111.

619 Burns, A. D., Frank, T., Hamill, I., Shi, J.-M., 2004. The Favre averaged drag model for  
620 turbulence dispersion in Eulerian multi-phase flows. *Proc. 5<sup>th</sup> Int. Conf. on Multiphase Flow*,  
621 ICMF2004, Yokohama, Japan.

622 Chapman, S. and Cowling, T. G., 1970. The Mathematical Theory of Non-uniform Gases,  
623 *Cambridge University Press*.

624 Clever, H. L., Battino, R., Miyamoto, H., Yampolski, Y. and Young, C. L. , 2014 IUPAC-NIST  
625 Solubility Data Series. 103. Oxygen and Ozone in Water, Aqueous Solutions, and Organic  
626 Liquids (Supplement to Solubility Data Series Volume 7). *Journal of Physical and Chemical*  
627 *Reference Data* 43, 033102.

628 Cockx, A., Do-Quang, Z., Audic, J., Line, A. and Roustan, M., 2001. Global and local mass  
629 transfer coefficients in waste water treatment process by computational fluid dynamics.  
630 *Chemical Engineering and Processing: Process Intensification* 40, 187–194.

631 Drew, D. A., Passman, S. L., 1998. Theory of Multicomponent Fluids, *Springer*.

632 Ferrell, R. T. and Himmelblau, D. M., 1967. Diffusion coefficients of nitrogen and oxygen in  
633 water. *Journal of Chemical and Engineering Data* 12, 111–115.

634 Gray, D. E. (Ed.), 1957. American Institute Of Physics Handbook, *McGraw Hill*.

635 Han, P. and Bartels, D. M., 1996. Temperature dependence of oxygen diffusion in H<sub>2</sub>O and  
636 D<sub>2</sub>O. *Journal of Physical Chemistry* 100, 5597–5602.

637 Himmelblau, D. M., 1964. Diffusion of dissolved gases in liquids. *Chemical Reviews* 64, 527–  
638 550.

639 Hlawitschka, M. W., Oßberger, M., Backes, C., Klüfers, P., and Bart, H.-J., 2017a. Reactive mass  
640 transfer of single NO bubbles and bubble bouncing in aqueous ferric solutions – A feasibility  
641 study. *Oil & Gas Science and Technology* 72, 11.

642 Hlawitschka, M., Kovats, P., Zähringer, K., and Bart, H.-J. , 2017b. Simulation and experimental  
643 validation of reactive bubble column reactors. *Chemical Engineering Science* 170, 306–319.

644 Hori, Y., Bothe, D., Hayashi, K., Hosokawa, S., and Tomiyama, A., 2020. Mass transfer from  
645 single carbon-dioxide bubbles in surfactant-electrolyte mixed aqueous solutions in vertical  
646 pipes. *International Journal of Multiphase Flow* 124, 103207.

647 Hosokawa, S., Tomiyama, A., Misaki, S. and Hamada, T., 2002. Lateral migration of single  
648 bubbles due to the presence of wall. *Proc. ASME Joint U.S.-European Fluids Engineering*  
649 *Division Conference, FEDSM2002*, Montreal, Canada.

650 Huber, M. L., Perkins, R. A., Laesecke, A., Friend, D. G., Sengers, J. V., Assael, M. J., Metaxa, I.  
651 N., Vogel, E., Mares, R. and Miyagawa, K., 2009 New International Formulation for the  
652 Viscosity of H<sub>2</sub>O. *Journal of Physical and Chemical Reference Data* 38, 101–125.

653 Ishii, M. and Hibiki, T., 2011. Thermo-fluid dynamics of two-phase flow. *Springer*, 2<sup>nd</sup> ed.

654 Ishii, M. and Zuber, N., 1979. Drag coefficient and relative velocity in bubbly, droplet or  
655 particulate flows. *AIChE Journal* 25, 843–855.

656 Kell, G. S., 1975. Density, thermal expansivity, and compressibility of liquid water from 0° to  
657 150°C: Correlations and tables for atmospheric pressure and saturation reviewed and  
658 expressed on 1968 temperature scale. *Journal of Chemical and Engineering Data* 20, 97–105.

659 Kipping, R., Kryk, H., and Hampel, U., 2020. Experimental analysis of gas phase dynamics in a  
660 lab scale bubble column operated with deionized water and NaOH solution under uniform  
661 bubbly flow conditions. *Chemical Engineering Science* 229, 116056.

662 Kovats, P., Thevenin, D., and Zaehring, K., 2018. Characterizing fluid dynamics in a bubble  
663 column aimed for the determination of reactive mass transfer. *Heat and Mass Transfer* 54,  
664 453–461.

665 Krauß, M. and Rzehak, R., 2017. Reactive absorption of CO<sub>2</sub> in NaOH: Detailed study of  
666 enhancement-factor models. *Chemical Engineering Science* 166, 193–209.

667 Krauß, M. and Rzehak, R., 2018. Reactive absorption of CO<sub>2</sub> in NaOH: An Euler-Euler  
668 simulation study. *Chemical Engineering Science* 181, 199–214.

669 Liao, J., Ziegenhein, T., and Rzehak, R., 2016. Bubbly flow in an airlift column: a CFD study.  
670 *Journal of Chemical Technology & Biotechnology* 91, 2904–2915.

671 Menter, F. R., 2009. Review of the shear-stress transport turbulence model experience from  
672 an industrial perspective. *International Journal of Computational Fluid Dynamics* 23, 305–316.

673 Merker, D., Böhm, L., Oßberger, M., Klüfers, P., and Kraume, M., 2017. Mass Transfer in  
674 Reactive Bubbly Flows – A Single-Bubble Study. *Chemical Engineering Technology* 40 1391–  
675 1399.

676 Mewes, D. and Wiemann, D., 2003. Two-phase flow with mass transfer in bubble columns.  
677 *Chemical Engineering Technology* 26, 862–868.

678 Parekh, J. and Rzehak, R., 2018. Euler-Euler multiphase CFD-simulation with full Reynolds  
679 stress model and anisotropic bubble-induced turbulence. *International Journal of Multiphase  
680 Flow* 99, 231–245.

681 Rettich, T. R., Battino, R. and Wilhelm, E., 2000. Solubility of gases in liquids. 22. High-precision  
682 determination of Henry's law constants of oxygen in liquid water from T=274 K to T=328 K.  
683 *Journal of Chemical Thermodynamics* 32, 1145–1156.

684 Roig, V. and Larue de Tournemine, A., 2007. Measurement of interstitial velocity of  
685 homogeneous bubbly flows at low to moderate void fraction. *Journal of Fluid Mechanics* 572,  
686 87–110.

687 Rzehak, R. and Krepper, E., 2013. Bubble-induced turbulence: Comparison of CFD models.  
688 *Nuclear Engineering and Design* 258, 57–65.

689 Rzehak, R. and Krepper, E., 2013a. CFD modeling of bubble-induced turbulence. *International  
690 Journal of Multiphase Flow* 55, 138–155.

691 Rzehak, R. and Krepper, E., 2015. Bubbly flows with fixed polydispersity: Validation of a  
692 baseline closure model. *Nuclear Engineering and Design* 287, 108–118.

693 Rzehak, R. and Kriebitzsch, S., 2015. Multiphase CFD-simulation of bubbly pipe flow: A code  
694 comparison. *International Journal of Multiphase Flow* 68, 135–152.

695 Rzehak, R., Krepper, E., Liao, Y., Ziegenhein, T., Kriebitzsch, S. and Lucas, D., 2015. Baseline  
696 model for the simulation of bubbly flows. *Chemical Engineering and Technology* 38, 1972–  
697 1978.

698 Rzehak, R., Krepper, E., 2016. Euler-Euler simulation of mass-transfer in bubbly flows.  
699 *Chemical Engineering Science* 155, 459–568.

700 Rzehak, R. 2016. Modeling of mass-transfer in bubbly flows encompassing different  
701 mechanisms. *Chemical Engineering Science* 151, 139–143.

702 Rzehak, R., Ziegenhein, T., Kriebitzsch, S., Krepper, E., and Lucas, D., 2017.  
703 Unified modeling of bubbly flows in pipes, bubble columns, and airlift columns.  
704 *Chemical Engineering Science* 157, 147–158.

705 Rzehak, R., Krauß, M., Kovats, P., and Zähringer, K., 2017a. Fluid dynamics in a bubble column:  
706 New experiments and simulations. *International Journal of Multiphase Flow* 89, 299–312.

707 Sander, R., 2015. Compilation of Henry's law constants (version 4.0) for water as solvent.  
708 *Atmospheric Chemistry and Physics* 15, 4399–4981.

709 Shi, P. and Rzehak, R., 2018. Bubbly flow in stirred tanks: Euler-Euler / RANS modeling.  
710 *Chemical Engineering Science* 190, 419–435.

711 Solsvik, J., 2018. Lagrangian modeling of mass transfer from a single bubble rising in stagnant  
712 liquid. *Chemical Engineering Science* 190, 370–383.

713 Taborda, M. A. and Sommerfeld, M., 2021. Reactive LES-Euler/Lagrange modelling of bubble  
714 columns considering effects of bubble dynamics. *Chemical Engineering Journal* 407, 127222.

715 Tomiyama, A., Kataoka, I., Zun, I., and Sakaguchi, T., 1998. Drag coefficients of single bubbles  
716 under normal and micro gravity conditions. *JSME International Journal B* 41, 472–479.

717 Tomiyama, A., Tamai, H., Zun, I., and Hosokawa, S., 2002. Transverse migration of single  
718 bubbles in simple shear flows. *Chemical Engineering Science* 57, 1849–1858.

719 Vargaftik, N. B., Volkov, B. N. and Voljak, L. D., 1983. International tables of the surface tension  
720 of water. *Journal of Physical and Chemical Reference Data* 12, 817–820.

721 Verhallen, P., Oomen, L., Elsen, A., Kruger, J. and Fortuin, J., 1984. The diffusion coefficients  
722 of helium, hydrogen, oxygen and nitrogen in water determined from the permeability of a  
723 stagnant liquid layer in the quasi-steady state. *Chemical Engineering Science* 39, 1535–1541.

724 Wagner, W. and Pruss, A., 2002. The IAPWS formulation 1995 for the thermodynamic  
725 properties of ordinary water substance for general and scientific use. *Journal of Physical and*  
726 *Chemical Reference Data* 31, 387–535.

727 Wise, D. and Houghton, G. 1966. The diffusion coefficients of ten slightly soluble gases in  
728 water at 10–60°C. *Chemical Engineering Science* 21, 999–1010.

- 729 Yeoh, G. H. and Tu, J. Y., 2010. Computational Techniques for Multiphase Flows — Basics and  
730 Applications, *Butterworth-Heinemann*.
- 731 Zhang, C., Yuan, X., Luo, Y., and Yu, G., 2018. Prediction of species concentration distribution  
732 using a rigorous turbulent mass diffusivity model for bubble column reactor simulation part I:  
733 Application to chemisorption process of CO<sub>2</sub> into NaOH solution. *Chemical Engineering  
734 Science* 184, 161–171.
- 735 Zidouni, F., Krepper, E., Rzehak, R., Rabha, S., Schubert, M., Hampel, U., 2015. Simulation of  
736 gas-liquid flow in a helical static mixer. *Chemical Engineering Science* 137, 476-486.
- 737 Ziegenhein, T., Rzehak, R., Krepper, E. and Lucas, D., 2013. Numerical simulation of  
738 polydispersed flow in bubble-columns with the inhomogeneous multi-size-group model.  
739 *Chemie Ingenieur Technik* 85, 1080–1091.
- 740 Ziegenhein, T., Rzehak, R., Lucas, D., 2015. Transient simulation for large scale flow in bubble  
741 columns. *Chemical Engineering Science* 122, 1-13.
- 742 Ziegenhein, T., Rzehak, R., Ma, T., and Lucas, D., 2017. A unified approach for modeling  
743 uniform and non-uniform bubbly flows. *Canadian Journal of Chemical Engineering* 95, 170–  
744 179.